

**Tuning magnetism and crystal orientations by octahedral coupling in LaCoO<sub>3</sub>/LaMnO<sub>3</sub> thin films**Xiangxiang Guan,<sup>1,2</sup> Xi Shen,<sup>1</sup> Jing Zhang,<sup>1,2</sup> Wei Wang,<sup>1,2</sup> Jine Zhang,<sup>1,2</sup> Huaixiang Wang,<sup>1,2</sup> Weipeng Wang,<sup>1</sup> Yuan Yao,<sup>1,2</sup> Junjie Li,<sup>1</sup> Changzhi Gu,<sup>1,2</sup> Jirong Sun,<sup>1,2</sup> and Richeng Yu<sup>1,2,\*</sup><sup>1</sup>*Beijing National Laboratory of Condensed Matter Physics, Institute of Physics, Chinese Academy of Sciences, Beijing 100190, People's Republic of China*<sup>2</sup>*School of Physics Sciences, University of Chinese Academy of Sciences, Beijing 100190, People's Republic of China*

(Received 2 February 2019; revised manuscript received 24 May 2019; published 22 July 2019)

(LaCoO<sub>3</sub>/LaMnO<sub>3</sub>)<sub>5</sub> multilayers with fixed LaMnO<sub>3</sub> thickness and varying LaCoO<sub>3</sub> thickness grown on SrTiO<sub>3</sub> (001) substrates are studied by scanning transmission electron microscopy at the atomic scale. Utilizing peak pairs analysis on annular bright field images, the precise atomic positions and the degree of octahedral rotation are obtained. Our study shows that the *c* axis of LaMnO<sub>3</sub> sandwiched by LaCoO<sub>3</sub> layers experiences a transition from the in-plane direction to the out-of-plane direction as the LaCoO<sub>3</sub> layer thickness increases, due to the oxygen octahedral coupling with LaCoO<sub>3</sub> layers. An abnormal suppression in saturation magnetization with increasing the thickness of the LaCoO<sub>3</sub> is observed and ascribed to the enhanced MnO<sub>6</sub> octahedral rotation. Our work provides a way to tune the magnetic properties of epitaxially grown thin films via interfacial octahedral engineering.

DOI: [10.1103/PhysRevB.100.014427](https://doi.org/10.1103/PhysRevB.100.014427)**I. INTRODUCTION**

The interface in transition metal oxides offers an excellent platform for exploring the entanglement effects of spin, orbital, charge, and lattice degrees of freedom. The entanglement of these four degrees of freedom gives rise to a variety of new phenomena, including two-dimensional electron gas, anomalous Hall effect, colossal magnetoresistance [1–3], etc. Recently, the correlation between magnetism and oxygen octahedral rotation and/or distortion at the interface has attracted considerable interest. For instance, by growing SrRuO<sub>3</sub> layers on compressive NdGaO<sub>3</sub> and tensile SmScO<sub>3</sub> substrates, Aso *et al.* revealed that the octahedral distortion of SrRuO<sub>3</sub> has an effect on the magnetotransport properties [4]. Also, Zhang *et al.* demonstrated that the elongation of the interfacial MnO<sub>6</sub> octahedron by coupling with the LaCoO<sub>2.5</sub> layer can cause the magnetic easy axis of the La<sub>2/3</sub>Sr<sub>1/3</sub>MnO<sub>3</sub> film to switch from the in-plane direction to the out-of-plane direction [5].

Among the transition metal oxides, LaMnO<sub>3</sub> (LMO) attracts intensive attention because of its ferromagnetic property in thin films, which is different from the A-type antiferromagnetic property in its bulk counterpart [6–9], and significant efforts have been devoted to investigating the effect of octahedral distortion on the magnetism in thin films. By reducing the oxygen pressure in the growth process, LMO on LaAlO<sub>3</sub> (100) exhibits magnetic enhancement due to the MnO<sub>6</sub> distortion decreasing [9]. According to theoretical calculations, strain-induced octahedral distortion provoking the change of orbital ordering can be employed for modifying the magnetism in the LMO thin film [10]. By analyzing the unique x-ray diffraction intensity profile of half-order peaks, Zhai *et al.* suggested that the interfacial MnO<sub>6</sub> octahedral

rotation in the LaMnO<sub>3</sub>/SrTiO<sub>3</sub> superlattice is responsible for ferromagnetism [11]. Consequently, oxygen octahedral engineering by heterogeneous interface has become an important approach to tuning the magnetism in the thin film system.

However, the annular bright field (ABF) study on the octahedral distortion and/or rotation in the LMO thin film by transmission electron microscopy (TEM) is rarely reported [12]. The reason may be ascribed to the complex structural properties of LaMnO<sub>3</sub>. For the bulk of LaMnO<sub>3</sub>, it has a typically orthorhombic structure with the *Pbnm* space group, which has a unit cell dimension of  $\sqrt{2}a_{pc} \times \sqrt{2}a_{pc} \times 2a_{pc}$ , where  $a_{pc}$  denotes the pseudocubic perovskite lattice parameter. For this reason, when epitaxially grown on a cubic (001)-oriented substrate, the LMO thin film usually forms a mixture of multiple domains, where the *c* axis lying in the in-plane [110]/[1 $\bar{1}$ 0] direction is mixed with the *c* axis along the out-of-plane direction. This is a common phenomenon in such a thin film with the orthorhombic structure of *Pbnm*. For example, three domains were reported to coexist in the orthorhombic LaFeO<sub>3</sub>-YMnO<sub>3</sub> multilayers [13]. It is suggested that the multidomain behavior in a thin film has become an obstacle to the investigation of the oxygen octahedron of the orthorhombic LMO thin film by the ABF technique. The epitaxial LaCoO<sub>3</sub> (LCO) thin film is ferromagnetic and has a Curie temperature of about 80 K [14]. Dark stripes are found to exist in the LCO thin film, which have a close relationship with the magnetism [15–17]. The magnetism of the LCO thin film is one order of magnitude weaker than that of the LMO thin film [18].

In this work, we obtain two separate orientations in LMO by grouping different thickness values of epitaxial LCO layer on a SrTiO<sub>3</sub> (001) (STO) substrate, as indicated by selected area electron diffraction (SAED) and high-angle annular dark-field (HAADF) images. This allows the advanced high-resolution ABF technique to be fully used to investigate the

\*rcyu@iphy.ac.cn

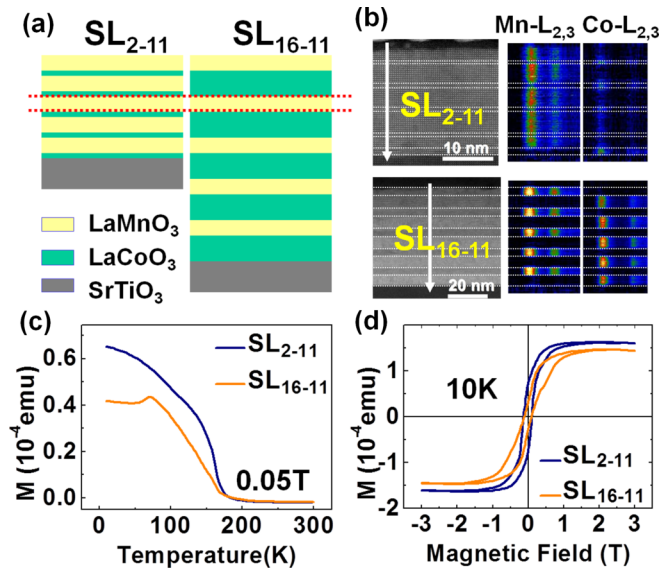


FIG. 1. (a) Schematic diagram of SL<sub>2-11</sub> and SL<sub>16-11</sub>, with red dotted lines indicating the same thick LMO layers in the two specimens. (b) HAADF image, EELS spectrum images of Mn-L<sub>2,3</sub> and Co-L<sub>2,3</sub> of SL<sub>2-11</sub> (upper) and SL<sub>16-11</sub> (lower), with white arrows indicating the positions and directions of EELS line scan. (c) Temperature dependence of magnetization with 0.05 T field cooling. (d) Hysteresis loops of the two samples.

details of oxygen octahedral rotation at the atomic level for the multilayers with different orientations. We also analyze the factors which affect the ferromagnetism in the LMO thin film. This work offers a path to tuning the magnetism of the LMO thin film.

## II. EXPERIMENT

### A. Sample fabrication and magnetization measurement

Using pulsed laser deposition, we fabricated multilayers (superlattices), each consisting of five LCO layers and five LMO layers which are alternately sandwiched. Specifically, one is composed of five 11-uc-thick LMO layers and five 2-uc-thick LCO layers, and the other is comprised of five 11-uc-thick LMO layers and five 16-uc-thick LCO layers (uc represents unit cell) on STO (001) substrates as illustrated in Fig. 1(a). The details of sample synthesis and the magnetization measurements were given in Ref. [18]. Note that all thin films were grown under the identical conditions, including oxygen pressure and the laser energy, except for the laser pulse times which are different for LCO layers with different thicknesses.

### B. TEM characterization

The SAEDs were acquired with an exposure time of 2.0 s in the TEM mode. The HAADF images were used to reveal the differences in distribution of orientations relating to SAEDs. The octahedral rotations in the LMO films were further investigated by ABF imaging along the pseudocubic [110]<sub>pc</sub> direction. The HAADF and ABF images were acquired simultaneously by utilizing a JEOL-ARM200F electron microscope

equipped with a cold field-emission electron gun and double Cs correctors for both the condenser lens and the objective lens. The convergence semiangle for the electron probe was 14–17 mrad. The ABF signals for the samples were collected from a detector angle range of  $\sim 11.5$ –23 mrad, and those for the HAADF images were 90–370 mrad. The spot size was chosen to be 8C, and the camera length was 6 cm.

To obtain the precise atomic position, the ABF images were denoised by the multivariate weighted principal component analysis routine (PCA Plugin in DIGITAL MICROGRAPH) developed by Watanabe and co-workers [19]. The atomic positions were determined by using the unit cell interpolation techniques in the “Motif detection” option (peak pairs analysis plugin in DIGITAL MICROGRAPH software; HREM Research Inc.) [20,21]. The octahedral rotation and the attached error bars were calculated by averaging 20 uc along the in-plane direction.

The electron energy-loss spectroscopy (EELS) line scans for mapping the interfaces were acquired in steps of 2 Å. Spot size was set to be 6C; each point had a duration time of 0.1 s to gain enough counts and good stability simultaneously. Dual EELS mode was selected to obtain the real-time zero-loss peaks for correcting the zero-loss peak drift and also for removing the plural scattering effect.

### C. ABF simulation

The ABF simulations of bulk LCO and LMO along the related directions were performed by using Multislice simulation with XHREM. Aperture radius was 20 mrad. Third-order and fifth-order Cs were 0.005 and 0 mm, respectively. The bright field angle of the detector was 20 mrad; the inner and outer angles of dark field were 10 and 20 mrad, respectively.

## III. RESULTS AND DISCUSSION

The schematic diagram of the [tuc-LCO/11uc-LMO]<sub>5</sub> superlattices ( $t = 2$  and  $t = 16$  denote SL<sub>2-11</sub> and SL<sub>16-11</sub>, respectively) grown on 3 mm × 5 mm × 0.5 mm (001)-oriented STO substrates is displayed in Fig. 1(a). The interfaces are discriminated by elemental maps of Mn L<sub>2,3</sub> and Co L<sub>2,3</sub> through using the EELS spectrum images after subtracting background and removing plural scattering [see Fig. 1(b)]. The total thickness value of LMO in SL<sub>2-11</sub> and that of SL<sub>16-11</sub>, counted with EELS, are exactly the same. Previously, we reported [18] that the measured magnetization of SL<sub>2-11</sub> is mainly from LMO, and SL<sub>16-11</sub> shows an antiferromagnetic transition at  $\sim 75$  K from field cooling temperature-dependent magnetization measurement as shown in Fig. 1(c), indicating an obvious magnetic contribution of LCO in SL<sub>16-11</sub>. Due to the interfacial magnetic coupling existing in thin films, we cannot accurately distinguish between the respective magnetic contribution from LCO and that from LMO. Because the thickness values of LMO in two multilayers are identical, if the magnetic contributions of LMO are the same, we can draw a conclusion: When an applied field is large enough, all spins of LCO in SL<sub>16-11</sub> will be redirected along the direction of the applied field; thus, the saturation magnetization in SL<sub>16-11</sub> should be larger than that in SL<sub>2-11</sub>, which is attributed to the additional magnetic

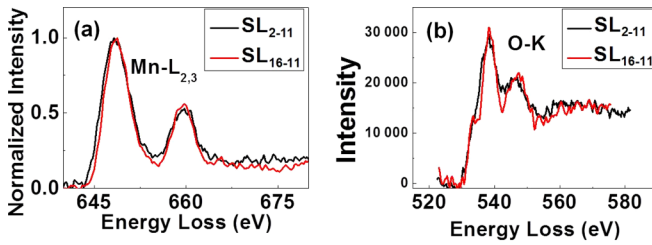


FIG. 2. (a) Normalized intensity plots of Mn- $L_{2,3}$  and (b) intensity plots of O- $K$  of LMO layers in  $SL_{2-11}$  and  $SL_{16-11}$ .

moment contributed from extra  $70[(16-2) \times 5] - uc$  thick LCO in  $SL_{16-11}$ . However, from the  $M-H$  curves [Fig. 1(d)] it follows that the total magnetization of  $SL_{16-11}$  is smaller than that of  $SL_{2-11}$ , but not larger than that of  $SL_{2-11}$  as expected. This result implies that the magnetic susceptibilities of LMO in  $SL_{2-11}$  and  $SL_{16-11}$  are different from each other, though their LMO thickness values are identical, and the magnetization of LMO in  $SL_{16-11}$  is smaller than that in  $SL_{2-11}$ .

Previous research indicated that a decrease in the ferromagnetism of the LMO thin film can be attained by octahedral distortion induced by several factors. The oxygen concentration in LMO is one of the factors [8,9]. Oxygen concentration in LMO can modify the out-of-plane lattice parameter, thus affecting the orbital ordering. In our films, by comparing the O- $K$  and Mn- $L$  peaks of  $SL_{2-11}$  with those of  $SL_{16-11}$  in EELS correspondingly (Fig. 2), no obvious changes are observed. It means that the oxygen concentration of LMO in  $SL_{2-11}$  and that in  $SL_{16-11}$  are similar to each other and thus cannot be the origin responsible for the difference in magnetism.

The second factor is lattice-strain-associated Jahn-Teller distortion [10,22]. In view of the lattice mismatch between the bulk LMO (orthorhombic  $Pbnm$  space group,  $a = 5.552 \text{ \AA}$ ,  $b = 5.727 \text{ \AA}$ , and  $c = 7.737 \text{ \AA}$ , pseudocubic  $a_{pc} = 3.916 \text{ \AA}$ ) [23] or the bulk LCO (rhombohedral  $R-3c$  space group,  $a = b = c = 5.342 \text{ \AA}$ , pseudocubic  $a_{pc} = 3.830 \text{ \AA}$ ) [24] and STO (cubic,  $a_{pc} = 3.905 \text{ \AA}$ ), the LMO bears a compressive strain with  $-0.282\%$  whereas LCO suffers a tensile strain of  $+1.921\%$  from the STO substrate. It is observed that the LMO layer retains the in-plane parameter identical with the one the STO substrate has, and no misfit dislocations are observed in either film (see the magnified images of Fig. 1(b) in the Supplemental Material, Fig. S1 [25]). Meanwhile, no splitting spots are found in the in-plane direction of the SAED in Fig. 3(a), nor in Fig. 3(b), confirming that both films are fully commensurate with a substrate with cube-on-cube-type epitaxy.

In the following, all the crystal indices in orthorhombic structure are marked by the subscript “O,” and those in pseudocubic structure by the subscript “pc.” All the relationships between pseudocubic and orthorhombic structures are shown in Fig. S2 [25].

Besides, it is worth noting that the  $\frac{1}{2}(0, 2m + 1, 2n)_{pc}$ , ( $m, n = \text{integer}; n \neq 0$ ) [circled in cyan in Fig. 3(a)] and  $\frac{1}{2}(0, 2i + 1, 2j + 1)_{pc}$ , ( $i \neq j = \text{integer}$ ) spots [circled in yellow in Fig. 3(a)] are present in SAED of  $SL_{2-11}$ , whereas the  $\frac{1}{2}(0, 2p, 2q + 1)_{pc}$ , ( $p, q = \text{integer}; p \neq 0$ ) spots [circled

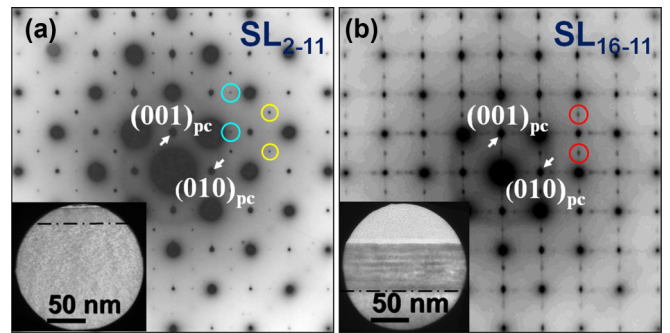


FIG. 3. The contrast inverted diffraction patterns of (a)  $SL_{2-11}$  and (b)  $SL_{16-11}$  recorded along the  $[001]_{pc}$  zone axis, with insets showing the low-magnification TEM images of selected areas.

in red in Fig. 3(b)] regularly appear in SAED of  $SL_{16-11}$ , signifying the different structures in the two films.

The inverse fast Fourier transforms (IFFTs) of these characteristic spots in fast Fourier transform (FFT) of HAADF images are presented in Figs. 4 and 5. The results show that the information about  $\{0, \frac{3}{2}, \frac{1}{2}\}_{pc}$  spots [circled in yellow in the inset of Fig. 4(a)], which are identical with the  $\{210\}_O$  spots along the  $[001]_{pc}$  zone axis of orthorhombic LMO with  $Pbnm$  space group ( $[001]_O$  for short), comes from the entire thin film of  $SL_{2-11}$  along the  $[001]_{pc}$  zone axis, accounting for the fact that the LCO layers are isostructural with the LMO layers. In fact, this orthorhombic structure is formed by in-phase octahedral rotations [22] as illustrated in the projection model and observed in the ABF in Fig. 4(c).

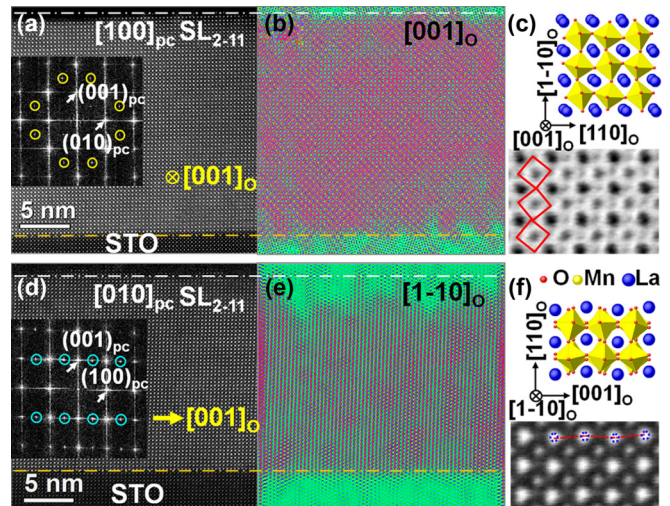


FIG. 4. HAADF images of  $SL_{2-11}$  viewed along the (a)  $[001]_{pc}$  zone axis and (d)  $[010]_{pc}$  zone axis, with insets showing their corresponding FFTs. IFFT images of (b) yellow spots in panel (a), and (e) cyan spots in panel (d), with pink marking the information area of selected spots, and green referring to positions with no signal. (c)  $[001]_O$ -zone view of octahedral rotation model for bulk LMO (upper) and magnified ABF image cut from LMO area (lower). (f)  $[1\bar{1}0]_O$ -zone view of octahedral rotation model for bulk LMO (upper), and magnified HAADF image cut from LMO area (lower) with blue dotted circles marking La ions, the red dashed lines between La ions representing misaligned La ions.

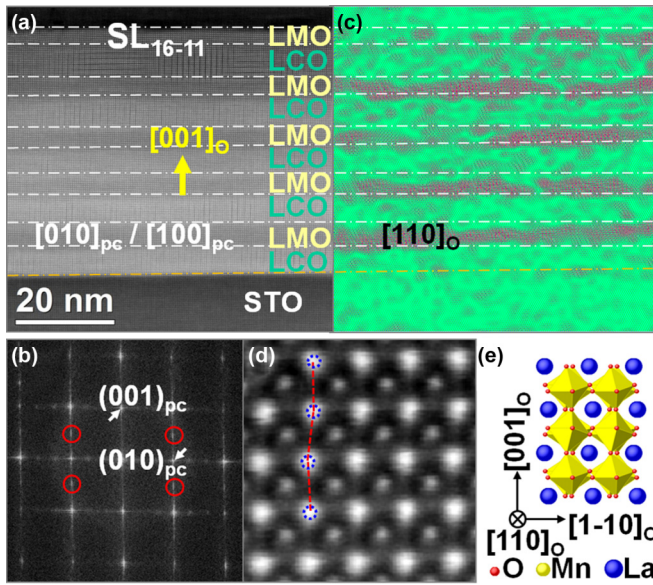


FIG. 5. (a) HAADF image of  $SL_{16-11}$  viewed along the  $[010]_{pc}/[001]_{pc}$  axis. (b) FFT of HAADF in panel (a). (c) Inverted FFT image of red circled spots in panel (b). (d) Magnified HAADF image cut from LMO area, illustrating La ions' displacements. (e)  $[110]_o$ -zone view of octahedral rotation model for bulk LMO.

Analogously, the spots  $\{\frac{1}{2}, 0, 1\}_{pc}$  and  $\{\frac{3}{2}, 0, 1\}_{pc}$  shown in the FFT of HAADF image of  $SL_{2-11}$  along the  $[010]_{pc}$  zone axis [cyan circle in the inset of Fig. 4(d)] are selected for IFFT. The IFFT shows the approximately whole film distribution to be similar to the result of the  $[001]_{pc}$  zone axis. The spots  $\{\frac{1}{2}, 0, 1\}_{pc}$  and  $\{\frac{3}{2}, 0, 1\}_{pc}$  represent the period  $c \approx 2a_{pc}$  of the orthorhombic structure. Corresponding La atoms shift upwards and downwards every other unit cell along the film plane which is equivalent to the  $[001]_o$  axis [see Fig. 4(f)].

The combination of the above with the observation along the  $[001]_{pc}$  zone axis indicates that LCO and LMO in  $SL_{2-11}$  are isostructural, exhibiting the orthorhombic  $Pbnm$  structure with the  $c$  axis parallel to the surface of the substrate. Moreover, two orthogonal cross-section observations demonstrate that the  $c/2$  [see the inset in Fig. 4(d)] and the interplanar distance of  $(1\bar{1}0)_o$  [see the inset in Fig. 4(a)] are the same and equal to  $3.905 \text{ \AA}$  of STO substrate. Thus, it is worth noticing that the LMO thin film in  $SL_{2-11}$  has a distorted orthorhombic structure due to the in-plane strain.

Compared with  $SL_{2-11}$ ,  $SL_{16-11}$  has a relatively sharp contrast between LCO and LMO, and the interfaces are marked by white short dash dots in the HAADF image shown in Fig. 5(a). As can be seen, the IFFT of the  $\{0, 1, \frac{1}{2}\}_{pc}$  spots [circled in red in Fig. 5(b)] reside merely at LMO layers. The  $\{0, 1, \frac{1}{2}\}_{pc}$  spots originate from the left and right arrangement of La atoms along the  $[001]_o$  direction [Fig. 5(d)], indicating that the orthorhombic  $c$  axis is along the out-of-plane direction [see Fig. 5(e)]. Moreover, there are a lot of horizontal dark stripes and vertical dark stripes scattered in LCO layers. The information about these dark stripes appears as the blurred spots between main diffraction spots, and these blurred spots are reflected on the FFT [as shown in Fig. 5(b)] and SAED in Fig. 3(b). In addition, both the  $[001]_{pc}$  axis and  $[010]_{pc}$  axis

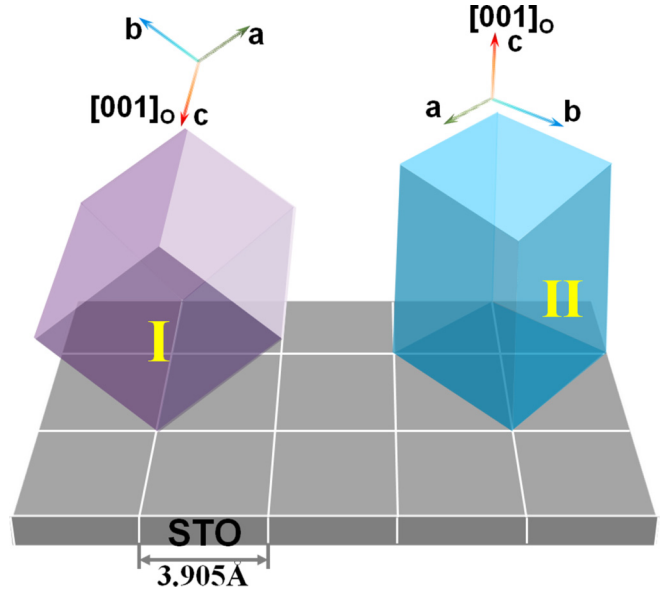


FIG. 6. Phenomenological model for  $SL_{2-11}$  (type I) (left) and  $SL_{16-11}$  (type II) (right) with orthorhombic  $c$  axis growing along the in-plane direction and out-of-plane direction, respectively.

have a similar morphology, indicating that the  $[001]_o$  in the LMO layer is perpendicular to the substrate in  $SL_{16-11}$ . Also, the lattice structure of LMO can be distorted by the in-plane strain confined by the substrate.

On the basis of the above results, the discrepancy between  $SL_{2-11}$  and  $SL_{16-11}$  can be described by the specifically selected crystal orientation in film growth as sketched in Fig. 6. Obviously, 2-uc LCO is not thick enough to generate the striplike structure as reported in many cobalt-based thin films [15–17]. Considering the interfacial diffusion in each interface, Co/Mn joint occupancy in LCO layers can be considered as a reason for the isostructure of LCO with LMO. It was reported that single-layer LMO with sufficient oxygen pressure has a tendency to be triflingly La deficient or Mn deficient, thus giving rise to the  $c$  axis in-plane growth, while single-layer LMO with low oxygen pressure causes the  $c$  axis to grow along the out-of-plane direction, accompanied by relaxation [8]. It is interesting that in our study, the  $c$  axis is in plane in  $SL_{2-11}$  while it is out of plane in  $SL_{16-11}$ .

In contrast, as the thickness of the LCO layer increases to 16 uc, the LCO can be expected to retain a striplike structure which is a common feature of single-layer LCO thin films [15–17]. The dark stripes are formed by enlarging the La-La interatomic distance and are usually accompanied by a small quantity of oxygen deficiency. In a previous study, we found that the number of dark stripes in a lanthanum cobalt oxide has a positive correlation with the measured ferromagnetism [26]. Thus, the observed dark stripes verify the magnetic contribution of LCO in  $SL_{16-11}$ .

The LCO with no stripes or with horizontal dark stripes has no influence on the in-plane lattice parameter of LMO, whereas vertical dark stripes in LCO have the highest possibility of affecting the La-La interatomic distance in LMO. Hence, we carefully check the in-plane La-La interatomic distances of LMO at interface especially near LCO with

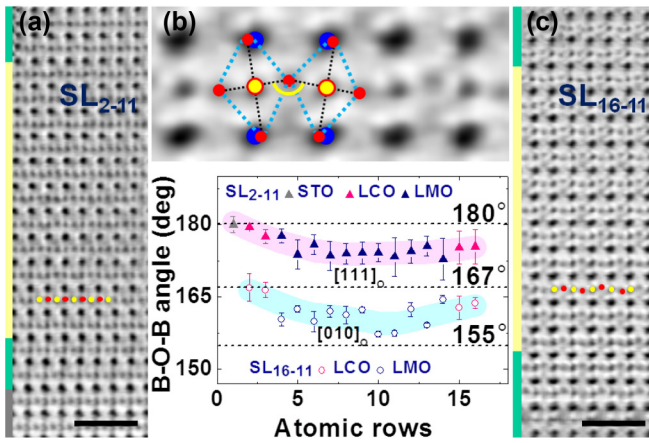


FIG. 7. ABF images of (a)  $SL_{2-11}$  and (c)  $SL_{16-11}$  along the  $[110]_{pc}$  direction, with gray, green, and yellow rims marking the regions of STO, LCO, and LMO, respectively. Data bar: 1 nm. (b) (upper) Yellow camber representing B-O-B angle, and (lower) in-plane B-O-B bond angle as a function of atomic row along out-of-plane direction for  $SL_{2-11}$  in panel (a) and for  $SL_{16-11}$  in panel (c), with pink and cyan curves representing the trend of B-O-B angle smoothed by the measured data.

vertical dark stripes (Fig. S3 in the Supplemental Material [25]), and confirm that the in-plane lattice of LMO coincides with that of STO. It means that the in-plane lattice strain is not the reason for the difference in magnetism between these two superlattices.

So far, the effect of oxygen concentration and lattice strain can be ruled out. The third factor that affects the octahedral distortion, and thus the magnetism, of LMO could be oxygen octahedral coupling.

Benefiting from the nonoverlapping oxygen along the B-O-B chains, the  $[110]_{pc}$  axis provides a significantly improved oxygen contrast for discussing the octahedral rotation. Figures 7(a) and 7(b) show the  $[110]_{pc}$ -ABF images of  $SL_{2-11}$  and  $SL_{16-11}$ , from which oxygen column positions marked by red dots are clearly seen. Owing to the different type of  $c$ -axis growth, we can conclude that the  $[110]_{pc}$  of  $SL_{2-11}$  and the  $[110]_{pc}$  of  $SL_{16-11}$  are equal to the  $[111]_O$  and  $[010]_O$  of LMO (see Fig. S2 [25]), respectively. As one can see from the results of the in-plane B-O-B angles, averaged values of  $175^\circ$  in  $SL_{2-11}$  and  $159^\circ$  in  $SL_{16-11}$  are larger than those in bulk-equivalent  $[111]_O$  ( $167^\circ$ ) and  $[010]_O$  ( $155^\circ$ ), respectively. The differences in Mn-O-Mn angle between the film and bulk are, respectively,  $7^\circ$  in  $SL_{2-11}$  and  $4^\circ$  in  $SL_{16-11}$ , which demonstrates that the octahedral rotation of LMO in  $SL_{2-11}$  is more strongly suppressed than that in  $SL_{16-11}$ . As is well

known, the existence of La or Mn vacancies in the LMO thin film causes a small number of  $Mn^{4+}$  ions to spread in the ocean of  $Mn^{3+}$  ions [7,9]. As is well known, the ferromagnetic exchange interaction depends sensitively on Mn-O-Mn bond angle [27]. Based on the analyses above, the more distorted in-plane bond angles for  $SL_{16-11}$  would reduce the probability of electron hops, and thereby inhibit the ferromagnetic order. This result coincides with the  $M$ - $H$  result discussed above.

Relative to the nonrotating Mn-O-Mn bond angle of  $180^\circ$ ,  $MnO_6$  octahedra show rotations to different extents, specifically  $5^\circ$  and  $21^\circ$ , in  $SL_{2-11}$  and  $SL_{16-11}$ , respectively. This difference originates from the octahedral coupling with the neighboring  $CoO_6$ . In  $SL_{2-11}$ , 2-uc-thick LCO next to the substrate is insufficient to overcome the energy gripped by the nonrotating  $TiO_6$  octahedron, thus giving rise to a slight rotating state in the upper coupled  $MnO_6$  octahedra, whereas for  $SL_{16-11}$ , the rotation of the  $MnO_6$  octahedron represents a highly distorted state by coupling with the highly rotated  $CoO_6$  like the scenario in oxygen-deficient  $LaCoO_{3-\delta}$  (see Fig. S4) [25].

Furthermore, the extent of octahedral rotation affects the  $A$ -site displacement and thus changes the orientation of LMO in growth. It unveils the mystery of the orientation switching sketched in Fig. 6. So far, we present the net octahedral coupling dominated switching of growth orientation of LMO, as well as the octahedral rotation mediated magnetism modification.

#### IV. CONCLUSIONS

In this study, the effects of LCO thickness on the magnetism and the octahedral network of epitaxial pulsed laser deposition grown  $[LaCoO_3(xuc)/LaMnO_3(11uc)]_5$  multilayers with  $x = 2, 16$  are studied in detail. An intuitive correlation between the octahedral rotation of LMO and the ferromagnetism is revealed by the ABF technique. Our study also predicts the orientation growth modification by means of interfacial oxygen octahedral coupling in an orthorhombic structure.

#### ACKNOWLEDGMENTS

This work was supported by the National Key Research Program of China (Grants No. 2016YFA0300701, No. 2017YFA0206200, and No. 2018YFA0208402) and the National Natural Science Foundation of China (Grants No. 11574376 and No. 11874413). X. Shen is grateful for the support from the Youth Innovation Promotion Association of CAS (2019009).

- [1] M. Bibes, J. E. Villegas, and A. Barthélémy, *Adv. Phys.* **60**, 5 (2011).
- [2] E. Dagotto, *Science* **318**, 1076 (2007).
- [3] H. Y. Hwang, Y. Iwasa, M. Kawasaki, B. Keimer, N. Nagaosa, and Y. Tokura, *Nat. Mater.* **11**, 103 (2012).
- [4] R. Aso, D. Kan, Y. Fujiyoshi, Y. Shimakawa, and H. Kurata, *Cryst. Growth Des.* **14**, 6478 (2014).

- [5] J. Zhang, Z. Zhong, X. Guan, X. Shen, J. Zhang, F. Han, H. Zhang, H. Zhang, X. Yan, Q. Zhang, L. Gu, F. Hu, R. Yu, B. Shen, and J. Sun, *Nat. Comm.* **9**, 1923 (2018).
- [6] X. R. Wang, C. J. Li, W. M. Lü, T. R. Paudel, D. P. Leusink, M. Hoek, N. Poccia, A. Vaillonis, T. Venkatesan, J. M. D. Coey, E. Y. Tsymbal, Ariando, and H. Hilgenkamp, *Science* **349**, 716 (2015).

- [7] C. Aruta, M. Angeloni, G. Balestrino, N. G. Boggio, P. G. Medaglia, A. Tebano, B. Davidson, M. Baldini, D. Di Castro, P. Postorino, P. Dore, A. Sidorenko, G. Allodi, and R. De Renzi, *J. Appl. Phys.* **100**, 023910 (2006).
- [8] J. Roqueta, A. Pomar, L. Balcells, C. Frontera, S. Valencia, R. Abrudan, B. Bozzo, Z. Konstantinović, J. Santiso, and B. Martínez, *Cryst. Growth Des.* **15**, 5332 (2015).
- [9] A. M. Zhang, W. C. Zhang, X. S. Wu, and J. G. Lin, *AIP Adv.* **7**, 055837 (2017).
- [10] B. R. K. Nanda and S. Satpathy, *Phys. Rev. B* **81**, 174423 (2010).
- [11] X. Zhai, L. Cheng, Y. Liu, C. M. Schleputz, S. Dong, H. Li, X. Zhang, S. Chu, L. Zheng, J. Zhang, A. Zhao, H. Hong, A. Bhattacharya, J. N. Eckstein, and C. Zeng, *Nat. Commun.* **5**, 4283 (2014).
- [12] M. A. Roldan, W. Salafranca, J. Salafranca, M. Varela, A. R. Lupini, S. J. Pennycook, and H. M. Christen, *Microsc. Microanal.* **19** (Suppl 2), 1916 (2013).
- [13] B. Pang, L. Sun, X. Shen, Y. Y. Lv, X. Li, F. X. Wu, S. H. Yao, J. Zhou, S. T. Zhang, and Y. B. Chen, *Materials* **10**, 839 (2017).
- [14] D. Fuchs, C. Pinta, T. Schwarz, P. Schweiss, P. Nagel, S. Schuppler, R. Schneider, M. Merz, G. Roth, and H. v. Löhneysen, *Phys. Rev. B* **75**, 144402 (2007).
- [15] J.-H. Kwon, W. S. Choi, Y.-K. Kwon, R. Jung, J.-M. Zuo, H. N. Lee, and M. Kim, *Chem. Mater.* **26**, 2496 (2014).
- [16] N. Biškup, J. Salafranca, V. Mehta, M. P. Oxley, Y. Suzuki, S. J. Pennycook, S. T. Pantelides, and M. Varela, *Phys. Rev. Lett.* **112**, 087202 (2014).
- [17] J. Gazquez, W. Luo, M. P. Oxley, M. Prange, M. A. Torija, M. Sharma, C. Leighton, S. T. Pantelides, S. J. Pennycook, and M. Varela, *Nano Lett.* **11**, 973 (2011).
- [18] J. Zhang, H. Zhang, X. Zhang, X. Guan, X. Shen, D. Hong, H. Zhang, B. Liu, R. Yu, B. Shen, and J. Sun, *Nanoscale* **9**, 3476 (2017).
- [19] M. Bosman, M. Watanabe, D. T. Alexander, and V. J. Keast, *Ultramicroscopy* **106**, 1024 (2006).
- [20] P. L. Galindo, S. Kret, A. M. Sanchez, J. Y. Laval, A. Yanez, J. Pizarro, E. Guerrero, T. Ben, and S. I. Molina, *Ultramicroscopy* **107**, 1186 (2007).
- [21] P. Galindo, J. Pizarro, S. Molina, and K. Ishizuka, *Microsc. Microanal.* **22**, 23 (2009).
- [22] Y. S. Hou, H. J. Xiang, and X. G. Gong, *Phys. Rev. B* **89**, 064415 (2014).
- [23] J. Rodríguez-Carvajal, M. Hennion, F. Moussa, A. H. Moudden, L. Pinsard, and A. Revcolevschi, *Phys. Rev. B* **57**, R3189 (1998).
- [24] G. Thornton, B. C. Tofield, and A. W. Hewat, *J. Solid State Chem.* **61**, 301 (1986).
- [25] See Supplemental Material at <http://link.aps.org/supplemental/10.1103/PhysRevB.100.014427> for more information.
- [26] Q. Q. Lan, X. Shen, H. W. Yang, H. R. Zhang, J. Zhang, X. X. Guan, Y. Yao, Y. G. Wang, R. C. Yu, Y. Peng, and J. R. Sun, *Appl. Phys. Lett.* **107**, 242404 (2015).
- [27] H. Nojiri, K. Kaneko, M. Motokawa, K. Hirota, Y. Endoh, and K. Takahashi, *Phys. Rev. B* **60**, 4142 (1999).